ADVANCED OPTICAL MATERIALS
www.advopticalmat.de

A Miniaturized Imaging Window to Quantify Intravital Tissue Regeneration within a 3D Microscaffold in Longitudinal Studies

Claudio Conci, Emanuela Jacchetti, Laura Sironi, Lorenzo Gentili, Giulio Cerullo, Roberto Osellame, Giuseppe Chirico, and Manuela Teresa Raimondi**

The biocompatibility assessment of biomaterials or the dynamic response of implanted constructs entails inflammatory events primary reflected in cell behavior at the microcirculatory system. Current protocols are based on histopathology which are over 40 years old and require the sacrifice of a huge number of laboratory animal with an unsustainable ethical burden of animal research. Intravital microscopy techniques are actually used to study implantation outcomes in real time. However, no device providing a specific tracking geometry to reposition the field of view of the microscope, for repeated analyses, exists yet. The synthetic photoresist SZ2080 is characterized here, allowing the development and in vivo validation of a miniaturized imaging window, the Microatlas, that, fabricated via two-photon polymerization, is implanted in living chicken embryos and imaged by fluorescence microscopy 3 and 4 days after the implant. The characterization of their elastomechanical and fluorescence properties highlights planar raster spacing as the most important parameter in tuning the mechanical and spectroscopic features of the structures. The quantification of cell infiltration inside the Microatlas demonstrates its potential as novel scaffold for tissue regeneration and as beacon for 3D repositioning of the microscope field of view and correction of optical aberrations.

1. Introduction

Most immunological response mechanisms (such as inflammation, allograft and xenograft preservation/reperfusion and rejection) are reflected by primary manifestations at the level of the microcirculatory system and as modifications in cell behavior.[1] The real time observation of these phenomena would give important information concerning biocompatibility of a medical device, biological function of engineered cellularized constructs, and tissue regeneration. Furthermore, a key requirement for a successful application of regenerated tissues is to assess their capability to induce an effective and functional vascularization when embedded into the surrounding host tissue.

To prove this outcome, histopathological inspections, by either visual[2] or digital analysis,[3] are still largely based on ex vivo standard staining (such as hematoxylin and eosin, Masson trichrome, Alcian Blue, and Oil red-O) aimed to evaluate the microscale environment of the excised tissue. Fibrotic capsule formation, inflammation,[4] presence of polymorphonuclear cells, giant cells, plasma cells, neovascularization, fatty infiltrates, fibrosis, and/or degradation of any implanted material,[5] up to a few months after the implant, are common examples of responses that regulative entities require to assess in order to evaluate the immunological reaction. This is the case for biocompatibility assessment of implantable biomaterials or therapeutic product testing for clinical approval.[6] Within these protocols, quantitative or semi-quantitative scoring systems have been used for a long time[7] and more recently standardized.[6] However, new technological developments aim at real intravital inspections,[8] greatly improving the quality and reliability of the assessment of the reaction to implants.[9] In fact, current protocols for the assessment of biomaterial biocompatibility, of their possible toxicity or of drugs vehiculation, to cite a few examples, are based on methods which are over 40 years old. In addition, these protocols require the sacrifice of at least three, for nonrodents, or five recipient animals, for rodents and from three to five different time points, resulting in a huge number of laboratory animal used for testing and an unsustainable ethical burden of animal research.

C. Conci, E. Jacchetti, L. Gentili, M. T. Raimondi
Department of Chemistry, Materials and Chemical Engineering
"Giulio Natta"
Politecnico di Milano
Piazza Leonardo da Vinci 32, Milano 20133, Italy
E-mail: manuela.raimondi@polimi.it

L. Sironi, G. Chirico
Department of Physics
Università di Milano-Bicocca
Piazza della Scienza 3, Milano 20126, Italy
E-mail: giuseppe.chirico@unimib.it

G. Cerullo
Dipartimento di Fisica
Politecnico di Milano
Piazza Leonardo da Vinci 32, Milano 20133, Italy

G. Cerullo, R. Osellame
Istituto di Fotonica e Nanotecnologie
CNR
Piazza Leonardo da Vinci 32, Milano 20133, Italy

The ORCID identification number(s) for the author(s) of this article can be found under https://doi.org/10.1002/adom.202101103.

DOI: 10.1002/adom.202101103

In order to optimize the biomaterial validation procedure and reduce the related costs, several attempts have been done to introduce intravital microscopy (IVM) techniques.[9,10] In fact, IVM can be used to quantify the subcutaneous neovascularization rate and the reaction to a foreign body,[11] also in terms of single cell behavior, by observing a single animal at multiple time-points, without the need of their sacrifice or repeated surgeries.[8] To this end, specific transparent observation chambers (i.e., window chambers) have been fabricated and implanted directly into the animal. These devices, though very versatile and useful in their applications, imply invasive, repeated, and unethical surgeries, leading to considerable stress and suffering of the animal. Moreover, during the first two weeks after implantation, the reaction due to the surgical procedure itself may be hardly distinguishable from the reaction elicited by the implant. In muscle and connective tissue, depending on the species and the severity of the surgical trauma, a steady state is seen in the cell population only after 9–12 weeks, inducing considerable delay in the evaluation protocol of a target material, such as a drug, a gel, or a biomaterial. In addition, the implantation window suffers from the impossibility of a micrometric repositioning of the microscope objective at each time point, not allowing the implementation of long-term evaluation protocols as required by the ISO/EN 10993-6 directive for the quantification of a biomaterial response.

To overcome these limitations, micrometric scaffolds have been placed inside those window chambers or in window-free mammalians (in relation to the inspected tissue district) to confine the inspected area.[8,11] These have a potentially double purpose: to create ectopic regenerative guides and to modulate the biological behavior down-to the single cell level. These scaffold-based devices have been fabricated using several techniques such as electrospinning, nanoimprinting, additive 3D printing of ceramics, metals and plastics together with other forms of bottom-up techniques.[12] For example, Dondossola and colleagues[8] employed micrometric scaffolds fabricated by using melt electrospinning writing of calcium phosphate-coated medical grade poly(ε-caprolactone) (mPCL-CaP) in a porous honeycomb geometry. However, the geometry of this scaffold had an average pore size of 100 μm, i.e., one/two orders of magnitude larger than the cellular scale. The same limitation affects the work of Lee and colleagues,[11] where an inverted colloidal crystal hydrogel scaffold was created with a precise microstructure that resembles decellularized bone but having a sub-millimetric size. In addition, none of these scaffolds provides a specific tracking geometry with a well-defined system of coordinates that would allow to perform repeated and prolonged IVM analyses. Moreover, these devices do not offer a truly 3D cellular environment because the host cells have to adhere into pores on the order of 100 μm in diameter, thus, to surfaces which are essentially 2D over the length scale of a single cell.[13]

In the last 15 years, advanced laser material processing techniques, based on ultrafast laser irradiation, have been developed to achieve mask-less and rapid microfabrication and micromachining of medical devices, e.g., stents,[14] lab-on-a-chip,[15] or scaffolds for tissue engineering.[16] The most advanced technology for fabricating ultraprecise scaffolds controlled at the cell scale is the direct laser writing, based on two-photon polymerization (2PP).[17,18] This rapid prototyping technology allows to overcome several limitations of the fabrication methods nowadays in use, such as the low spatial resolution (>100 μm) of additive printing and electrospinning or the poor control of the porosity of the structures fabricated through nanoimprinting. In addition, 2PP allows the fabrication of high aspect ratio polymeric structures of arbitrary 3D geometry with a spatial resolution down to 0.1 μm,[19] thus enabling the creation of 3D microenvironments for cell cultures. In fact, 2PP-fabricated scaffolds for tissue engineering offer cell adhesion sites in truly 3D microenvironments, spatially distributed similarly to those present in living tissue.[13]

The downscaling process employed in building functional structures should be combined with an effort to adapt them for IVM analysis. Biocompatible materials having specific optical properties, namely dim fluorescence and scattering signals, and suitable mechanical responses should be developed and used for 2PP fabrication. Up to now, few studies reported and verified mechanical and optical properties of two-photon polymerized material, even fewer in the context of implantable scaffolds or IVM applications.[20–27]

The determination of the mechanical properties of the scaffold and the ability to control them in the fabricated microstructure are requirements for the development of miniaturized window chambers. These chambers, aiming at long-term IVM analysis, are invaluable tools for the innovative in vivo biomaterials testing procedures and for tissue regeneration in general. Usually, the mechanical properties of a photoresist depend on the laser fabrication parameters (writing velocity, polymerized lines distance, laser power, etc.) that heavily influence material stiffness.[28] In fact, increasing the laser power and changing intervoxel spacing both in the XY (longitudinal plane) and Z (transversal plane) direction affect the material degree of polymerization and, as a consequence, its Young's modulus.[29,30]

In this paper, we introduce an innovative and miniaturized imaging window for intravital nonlinear microscopy, the Microatlas, implantable sub-cute and inspectable without the need of a percutaneous accesses. The Microatlas is fabricated by 2PP of the SZ2080 acrylic photoresist[31] and it is here characterized from the elastomechanical and optical point of view. With the purpose of optimizing the Microatlas in terms of both autofluorescence and mechanical properties (Young's modulus), we identified a set of parameters (writing power, step sizes, etc.) controllable during 2PP fabrication. The dependence of the elastomechanical properties of the fabricated structures on the fabrication parameters was evaluated by microindentation experiments and the autofluorescence of the Microatlas was characterized by two-photon microscopy. Finally, we implanted the Microatlas in live chick embryos ex ovo and we imaged the devices under confocal and two-photon microscopy, to quantify features of cell repopulation within the device.

2. Results and Discussion

The Microatlas was developed with the aim to produce a low invasive window chamber allowing intravital fluorescence time lapse imaging while fostering the in situ neovascularization, around and inside the 3D microstructured scaffolds and constituting an in situ artificial beacon for image resolution optimization

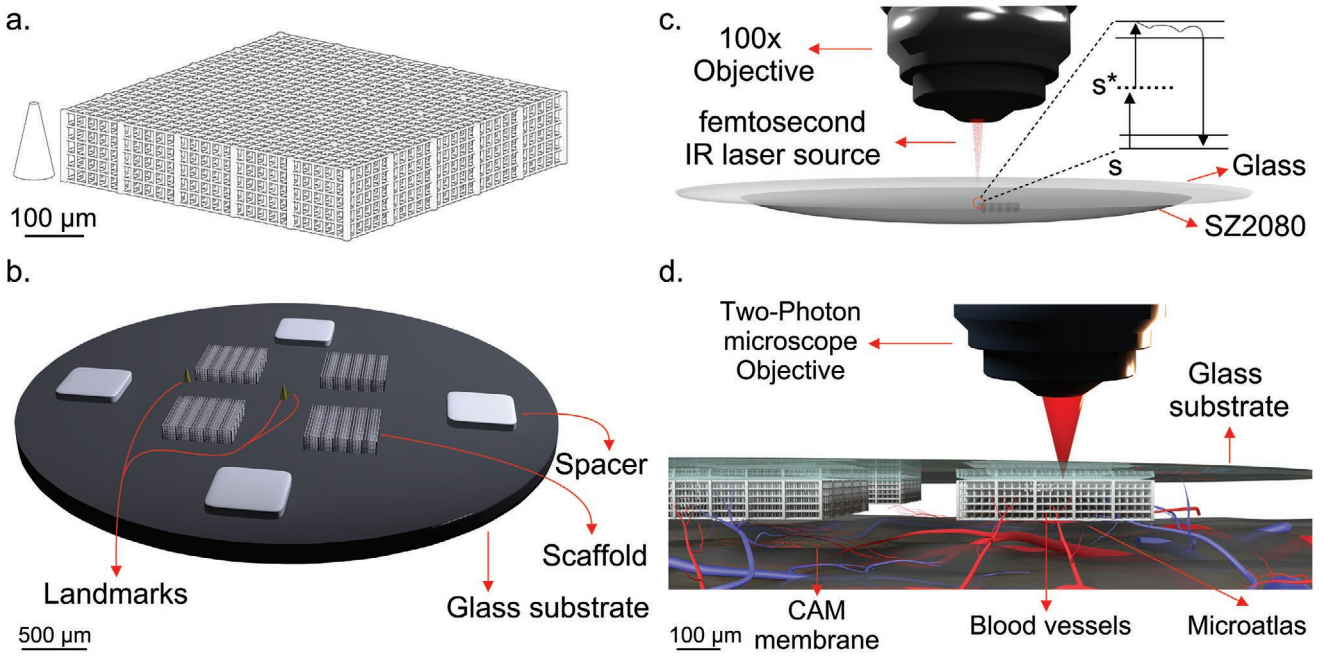

Figure 1. Sketched and rendering representation of the concept. a) Sketched representation of a laser written microscaffold (Atlas) for cell invasion. The Atlas, paired to the reference cone that allows vertical repositioning of the microscope field of view during intravital microscopy acquisitions, is assembled in the Microatlas. The overall size is $500 \times 500 \times 100\ \mu m^3$, with a cubic pore side of 20 µm. b) 3D rendering of the overall Microatlas device, laser written on a glass coverslip. The glass coverslip has been microstructured with a central 2×2 array of Atlas microstructures, symmetrically flanked by four spacers, landmarks for vertical repositioning and landmarks for planar repositioning of the microscope field of view. c) Rendering scheme of the two-photon polymerization. By using a high-numerical aperture (NA) and high-magnification objective, paired to a pulsed femtosecond laser source, we achieve a submicrometric resolution, beyond the diffraction limit, in the photosensitive biocompatible resist SZ2080. d) Rendering representation of the ex ovo implantation setup. The device was laid upon the chorioallantoic membrane (CAM). No conditioning factors were administered. The aim of the device microscaffold is to guide blood vessels regeneration.

(**Figure 1**). In order to fabricate our platform, we chose as photoresist the SZ2080 acrylic resin,[31] which has been proven to be biocompatible.[23,32] The microstructures fabricated with SZ2080 show a variable fluorescence signal[25,33] that is modulated by the type of photoinitiator used and the post-treatment, as recently outlined in ref. [34]. To characterize the mechanical properties of the structures, we photopolymerized several bulky parallelepipeds (**Figure 2**a), by varying fabrication parameters that modulate the energy dose released to the photoresist and, as a consequence, change its degree of reticulation, resulting in a variation of its mechanical and optical properties. The tested fabrication parameters are: the writing step size on the focal plane (R) and along the vertical axis (Z) (Figure 2b,c), and the laser power, P. Due to the polymerized voxel size achievable with our 2PP setup, ≅250 nm in the transverse plane and ≅1 µm in the longitudinal dimension, we chose an intervoxel spacing R in the range of 0.15–0.95 µm and Z in the range 0.5–2.0 µm. The elastic modulus, E, was derived from the analysis of the indentation-force/deformation curves.[35] Irrespective of the value of the writing power, P, and the step size along Z, we always found a linear decrease of E as a function of R (Figure 2d,e) with a slope of $\frac{\partial E}{\partial R}\Big|_{\substack{Z=0.5\mu m \\ Z=11.0\mu m}} \cong -1.7\frac{GPa}{\mu m}$, indicating that by reducing the voxels superposition in the focal plane, the material stiffness significantly decreases.

However, as we can see from Figure 2d,e, the elastic modulus depends also on the Z and P parameters. In fact, the laser writing power induces a change of 50% in the $\frac{\partial E}{\partial R}\Big|_{\substack{z \\ P}}$ slope (from $-1.9\frac{GPa}{\mu m}$ at $P = 6$ mW to $-1.1\frac{GPa}{\mu m}$ at $P = 4$ mW, at $Z = 0.5$ µm). On the contrary, the $\frac{\partial E}{\partial R}\Big|_{\substack{Z \\ P}}$ can reach values as high as $-2.5\frac{GPa}{\mu m}$ for $Z = 1.0$ µm and $P = 4$ mW, implying that an increase by 0.2 µm in the writing step R induces a decrease of about 0.5 GPa in the Young modulus of the fabricated structures. Moreover, there is a strong coupling of the Z and R parameters: the larger is Z, the steeper is the dependence of E on the writing step R. This can be easily derived by comparing Figure 2d, from which we measure $\frac{\partial E}{\partial R}\Big|_{\substack{Z=0.5\ \mu m \\ P=4\ mW}} = -1.1\frac{GPa}{\mu m}$ with Figure 2e, in which $\frac{\partial E}{\partial R}\Big|_{\substack{Z=1.0\ \mu m \\ P=4\ mW}} = -2.5\frac{GPa}{\mu m}$. Indeed, the parallelepipeds written with $Z = 2.0$ µm, exhibited sliding and collapses during the testing procedure.

In conclusion, our results identified a well-defined protocol for controlling the Young's modulus of the fabricated microstructures in which R appears to be the dominant parameter, in general agreement with other studies on different materials.[20,26] In fact, even if the literature studies adopted writing protocols with smaller intervoxel distances, they invariably reported similar dependences of the rigidity on the writing steps R and Z. The power level of the writing laser influenced

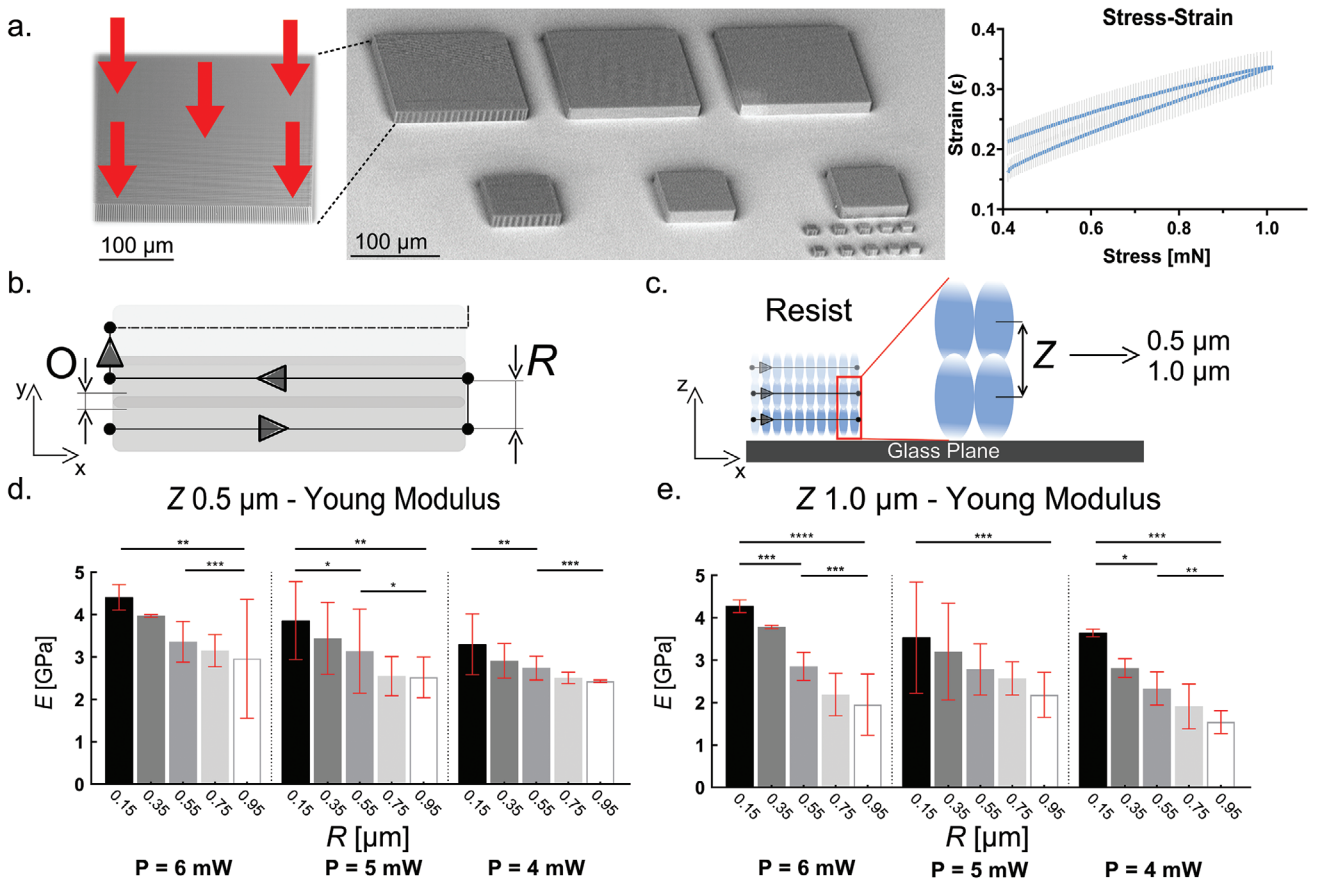

Figure 2. Structural and elastic features of the laser-written microstructures. a) Scanning electron microscopy (SEM) image of different "bulky" blocks realized by the two-photon polymerization. Left blow-up: SEM zoomed image of a single block highlighting the positions chosen for nanoindentation ($150 \times 150 \times 10\ \mu m^3$). Five different compression tests were realized per sample by using a nanoindenter. Right blow-up: A representative Stress–strain curve obtained per specimen. Each curve is averaged on five acquisitions. b) Sketch of the raster-scanning fabrication protocol in the focal (x–y) plane. Each "bulky" block was fabricated by polymerizing raster written lines spaced by R nm. Depending on the laser spot size, by decreasing the R parameter, we increase the overlapping region size (O) and the density of the microstructure. c) Three slices spaced by Z, were fabricated along the vertical direction. d,e) Dependence of the Young modulus upon the raster parameter R, for two slicing conditions ($Z = 500$ and $Z = 1000$ nm) and as a function of 2PP laser power. Data are linearly fitted as follows: $\frac{\partial E}{\partial R}\Big|_{\substack{P=6\,mW \\ Z=0.5\,\mu m}} = -0.0019 \pm 2.7310^{-4}\,(R = 0.941)$, $\frac{\partial E}{\partial R}\Big|_{\substack{P=5\,mW \\ Z=0.5\,\mu m}} = -0.00176 \pm 2.5210^{-4}\,(R = 0.941)$, $\frac{\partial E}{\partial R}\Big|_{\substack{P=4\,mW \\ Z=0.5\,\mu m}} = -0.00107 \pm 1.7010^{-4}\,(R = 0.929)$, $\frac{\partial E}{\partial R}\Big|_{\substack{P=6\,mW \\ Z=1.0\,\mu m}} = -0.00311 \pm 3.1710^{-4}\,(R = 0.969)$, $\frac{\partial E}{\partial R}\Big|_{\substack{P=5\,mW \\ Z=1.0\,\mu m}} = -0.00176 \pm 7.9510^{-5}\,(R = 0.993)$, $\frac{\partial E}{\partial R}\Big|_{\substack{P=4\,mW \\ Z=1.0\,\mu m}} = -0.00256 \pm 2.9410^{-4}\,(R = 0.953)$.

the material stiffness only,[36] in agreement with our finding that at most a 50% increase of the elastic modulus can be induced by increasing the writing power from 4 to 6 mW, while, when increasing the writing power to 7 mW, the structures start to degrade due to the excessive energy accumulation. Wider range of powers could be inspected in the cited literature works[20] by reducing the amount of photoinitiator added to the photoresist or by using pulse widths down to 100 fs.

In contrast with the elastomechanical properties, the effect of the writing parameters on the autofluorescence intensity of the fabricated structures, such as tissue engineering scaffolds, has not been widely investigated in research works to date. The control of the autofluorescence emission of a polymeric scaffold used for intravital applications is essential to allow fluorescent investigation of cell cultures, since too large autofluorescence levels limit the possibility of single cell identification during tissue regeneration. The autofluorescence intensity can be reduced by choosing specific types and concentrations of photoinitiators for the SZ2080 polymer or even avoiding their use at the expense of a considerable reduction of the processing window to produce high quality 3D microstructure.[33] Therefore, we thoroughly investigated the effect of the R, Z, and P parameters on the autofluorescence of the microfabricated structures (**Figure 3**). The study of the fluorescence intensity and spectral features identifies again the XY writing step R as the most effective parameter in modulating the autofluorescence signal. We see a clear decrease of the fluorescence intensity as R increases only for large values

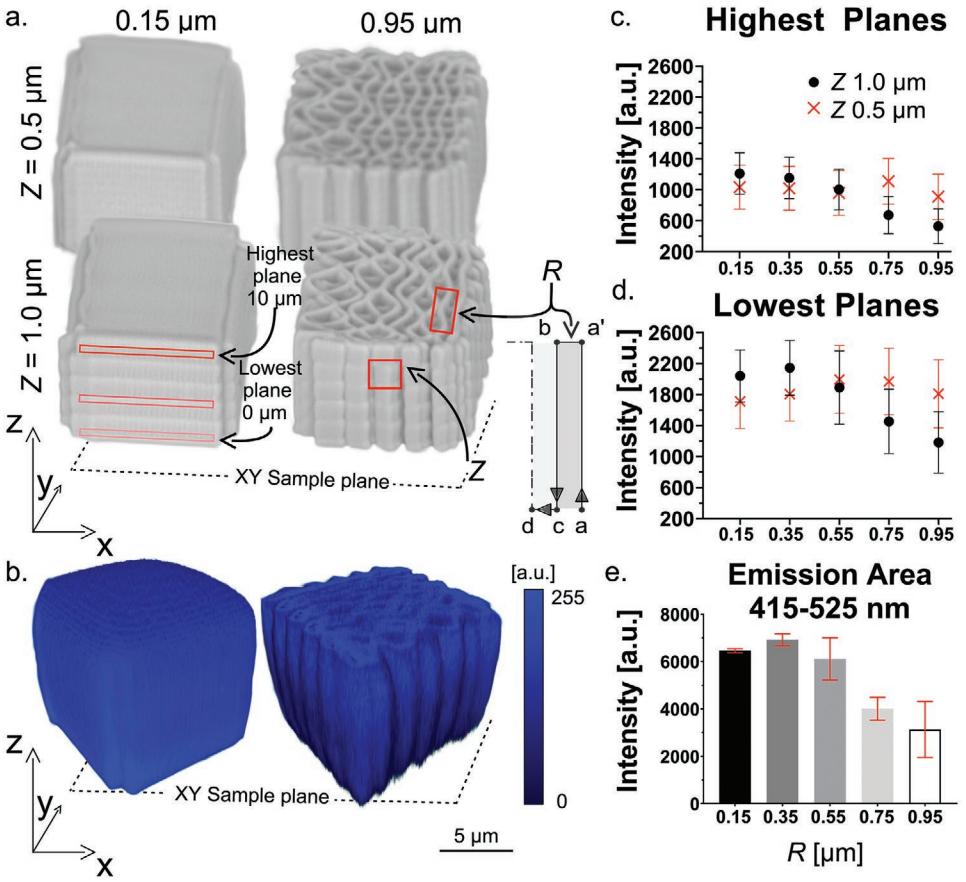

Figure 3. Confocal fluorescence microscopy. a) SEM images of 2PP "bulky" structures (size $10 \times 10 \times 10$ µm^3) test for confocal fluorescence imaging. On the lower left side, the red boxes highlight the chosen sample planes for autofluorescence analyses. On the right, detailed sections of the raster and sliced scanned fabrication approach. b) 3D rendering of the microstructures ($R = 0.150$ µm, left, $R = 0.950$ µm, right) as derived from the autofluorescence confocal Z-stack images. c,d) Maximum intensity value of the "bulky" blocks autofluorescence emission as a function of the raster parameter R, measured at the highest and lowest planes, respectively (excitation wavelength = 405 nm). e) Integrated area of the emission spectrum collected on "bulky" blocks as a function of the raster parameter.

of $Z = 1.0$–2.0 µm, a situation in which the structure is more similar to a porous than to a "semi-bulk" material because the intervoxel spacing is too wide to allow fusion of the polymerized lines (Figure 3a,b). Instead, with low Z and R values (i.e., $Z < 1.0$ µm and $R < 0.25$ µm), the structure could be defined as a "compact" material. These two situations, porous versus compact structures, elicit different interactions with light that can undergo stronger absorption (on the more compact structures) or stronger scattering (on the more porous structures), leading in any case to an intensity loss if a bulk structure must be optically sectioned. The observed intensity loss further depends on the distance of the observation plane from the supporting glass slide (Figure 3c,d). This could be easily explained by optical thickness considerations arising either from absorption or scattering induced by the structure. Therefore, to obtain a homogenous analysis of the whole samples, the central plane was taken as the standard for the analyses of the autofluorescence comparison. As reported in Figure 3c,d, the autofluorescence intensity decreases with R with a negative slope whose magnitude increases with Z. The overall decrease of the autofluorescence with R ($\Delta R = 0.8$ µm) in all planes was 46% ± 5% for $Z = 0.5$ µm and 49% ± 6% in the case of $Z = 1.0$ µm. The finding that the fluorescence signal loss with the penetration depth in the bulky structures does not depend on the spectral range chosen for the analysis (Figure 3e) seems to indicate that no massive scattering of the infrared light used to prime 2PP fluorescence is arising from the microstructure.

Once defined the polymerization parameters, we fabricated the Microatlas by 2PP (**Figure 4**a,b, see the Supporting Information). The device contains a combination of microscaffolds shaped as grids with square openings of 20 µm side, comparable to the cell dimension, and unique microobjects as 3D reference, which serve as beacons for repeated, long-time IVM observations (see also Figure 1c). The microgrids disposition (Figure 4b) allows to 3D reposition the field of view for repeated intravital observations of cells by fluorescence microscopy, avoiding the need of multiple histopathological analyses (Figure 1d). The skeleton, intended as the inner lattice of each scaffold grid, was polymerized first. We opted for $R = 0.25$ µm as the optimal choice leading to stable and perfectly reproducible skeletons with XY writing speed of 3 mm s^{-1}. The writing speed along the Z direction was lowered to 1 mm s^{-1} to reduce the time required for the frequent acceleration and deceleration in writing the short lines in this direction. The

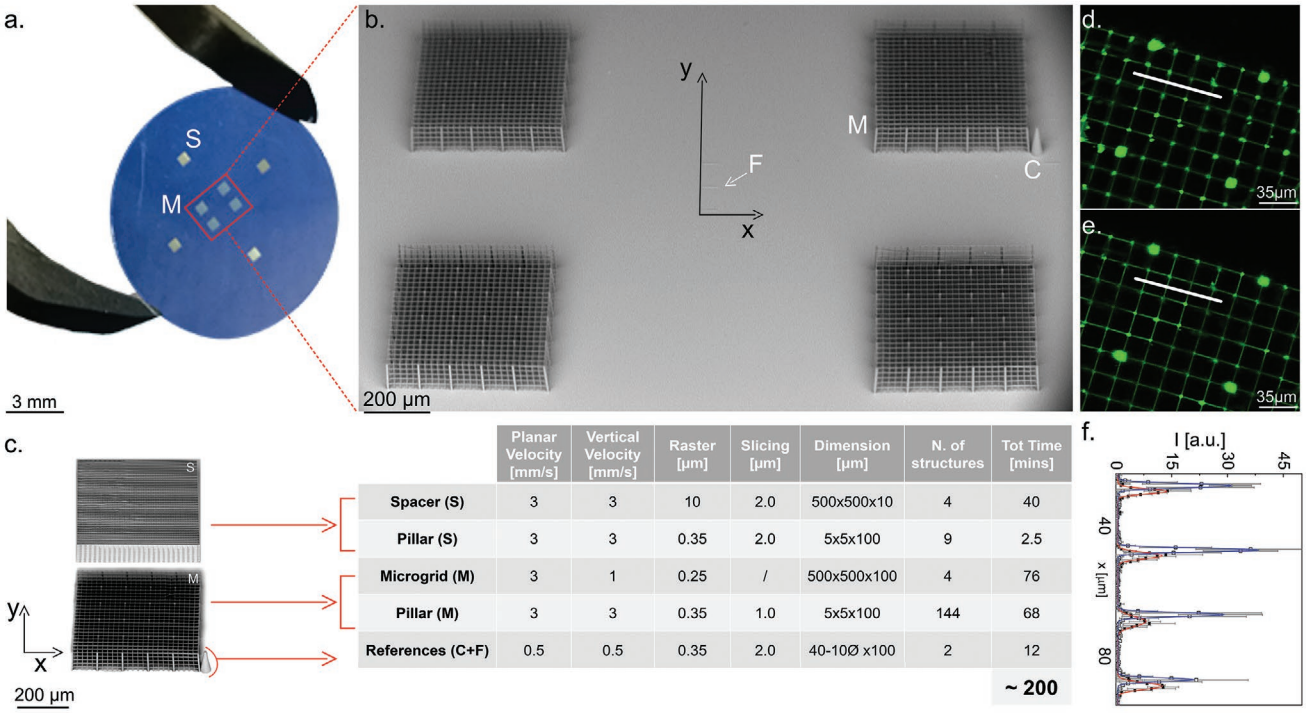

	Planar Velocity [mm/s]	Vertical Velocity [mm/s]	Raster [µm]	Slicing [µm]	Dimension [µm]	N. of structures	Tot Time [mins]
Spacer (S)	3	3	10	2.0	500x500x10	4	40
Pillar (S)	3	3	0.35	2.0	5x5x100	9	2.5
Microgrid (M)	3	1	0.25	/	500x500x100	4	76
Pillar (M)	3	3	0.35	1.0	5x5x100	144	68
References (C+F)	0.5	0.5	0.35	2.0	40-10Ø x100	2	12
							~ 200

Figure 4. 2PP writing parameters. a) Image of the 2PP Microatlas on a 12 mm (∅) glass coverslip. The four Atlas microstructures are written at the center of the glass slide. b) SEM (5 kV) images of the four Atlas microstructures with the details of the pillars, the grid geometry and all the reference structures, the cone (C) and the planar reference lines (F). c) Summary of the fabrication parameters for each of the features of the Microatlas: the Atlas (three lower rows and SEM image) and the spacer (two upper rows and SEM image) with the corresponding fabrication time. d) Two-photon image of the Atlas in 2% intralipid suspension with no phase correction. e) The same Atlas acquired at optimal phase correction (Zernike n. 5 and 11). f) Fluorescence profiles along the white line in panels (d) and (e) for no aberration correction (filled square and red curve) and for optimal aberrations corrections (open squares and blue curve). The solid curves are multi-Gaussian fit to the data.

skeleton fabrication was completed in 19 min (Figure 4d). Thicker columns, herein called Pillars, were added every 100 µm, along the XY plane, to assure Microatlas stability. For these structures, the writing speed was set at 3 mm s^{-1}, while $R = 0.35$ µm and $Z = 1.0$ µm were chosen. The 36 Pillars constituting the Microatlas microgrid required an overall fabrication time of almost 17 min (Figure 4d). Four spacers (Figure 4a), were fabricated with a dense woodpile configuration (lattice unit = $10 \times 10 \times 2$ μm^3) at the scan speed = 3 mm s^{-1}. To compensate possible structural collapses, loose Pillars ($R = 0.35$ µm, $Z = 2.0$ µm) were superimposed every 250 µm along each spacer side. Each Spacer, comprising the polymerized Pillars required almost 12.5 min fabrication time (Figure 4d). Finally, cones and the landmarks were fabricated in specific portion of the imaging window. Laser power fluctuations and imperfections of the baked photoresist played a determining role in the cone polymerization. Therefore, some burnt area may be present at the cone apex where it is more difficult to control the amount of deposited energy. The fabrication times, at least for the Microatlas microgrid, could be further reduces by adopting a parallel writing protocol based on a spatial light modulator (SLM), as recently done by our group.[37]

Other miniaturized imaging window has been reported in the literature.[8,11] Dondossola et al.[8] offered an unprecedented visualization of the reaction to biomaterials (electrospun fibers) implanted sub-cute in mice by means of a skin-folder chamber for up to 14 d. Nonlinear excitation imaging (fluorescence, second and third harmonics) allowed to visualize fibrotic reaction and angiogenesis. More recent studies have focused on the possibility to implant microdispensers (volume = $4 \times 0.8 \times 0.8$ mm^3) of anticancer drugs and to visualize their cytotoxic effect ex vivo[38] and in vivo, both with endoscopic confocal[39] and two-photon microscopy.[40] Differently from these reported cases, our Microatlas platform encompasses on a smaller area (Figure 4a) a bioengineered interface between the material to be tested and the host, together with a microscopic autofluorescent scaffold system that guides tissue regeneration and, in parallel, acts as a 3D reference for IVM. Moreover, our regular structures of the Microatlas can act as a fluorescent beacon to implement correction of aberrations induced by the hosting tissue.

The possibility to implement adaptive optics corrections in raster scanning setups for nonlinear microscopy was first reported in 2000[41] exploiting an intensity-based sensor-less method for two-photon raster scanning microscopy. Débarre and colleagues[42] substantially improved this scheme and demonstrated the feasibility of SLM-based aberration correction of two-photon images of biological specimens. However, these studies were based solely on the steep dependence of the two-photon fluorescence emission on the laser intensity and searched for a diffuse increase of the signal over large patches of the image. By employing the Microatlas geometry we can

improve directly our resolution on the fine features of the atlas. To test this possibility, we have taken two-photon autofluorescence images of a Microatlas skeleton in turbid media. Intralipid (20%) was dissolved at a final concentration of 2% in water and used as immersion medium for the two-photon excitation imaging (the working distance of the objective is 2 mm). The loss in spatial resolution induced by the presence of the turbid medium can be restored by compensating a few Zernike components of the field by means of an SLM inserted in a 4f configuration in the optical path of the two-photon microscope[43] (see Figure S0, Supporting Information). We could improve the spatial resolution of the images by acting only on the modes 5 (astigmatism-x) and 11 (primary spherical), as seen in Figure 4. The optical width (full width at half maximum (FWHM)) of the skeleton beams changes, from 2.1 ± 0.4 to 1.04 ± 0.06 μm, upon modes correction (Figure 4f). Given a nominal width of 0.47 μm of these features, we can estimate a corrected point spread function FWHM of 0.9 ± 0.06 μm.

To prove the Microatlas efficacy in a biologically relevant environment, we performed an implantation ex ovo using a modified protocol of the well-established chorioallantoic membrane (CAM) assay at different time points. In fact, the CAM is easy to manipulate during the grafting procedure and completely optically accessible during the whole microscopy analysis (Figure 4).[44–47] The chicken-embryo is a well-studied and cost-efficient model organism profiting from the great potential of intravital manipulation techniques.[48] Blood vessels can be analyzed in terms of the number, diameter, density, permeability, branch point number, and blood flow.[44,47,49] Despite its embryonic and nonmammalian nature, this is a perfect model to validate our device in vivo:[50] having a fast angiogenic response, like that occurring in mammalian tumors,[44] it allowed us to observe, in few days, a host response comparable to that obtainable in mice in weeks.

We employed two-photon, second harmonic generation (SHG), and confocal fluorescence microscopy analyses to study the host response to implantation of the Microatlas (**Figures 5** and **6**). We compared images acquired from three chicken embryos implanted with the Microatlas with images acquired from three unimplanted controls (Figures 5c,d). Our results showed that no infiltration occurred inside the Microatlas scaffolds until the third day after implant (Figure S1, Supporting Information). Then, confocal analyses showed that the tissue density in the control regions increased by 1.8 ± 0.1 times from day 3 to day 4, due to the continuous growing of the CAM membrane. Even though the infiltration in the Microatlas was delayed by almost 2 d, the increase of the localized cellular density in the Microatlas at day 3 and 4 from implantation was 4.4 ± 0.4 times more than for untreated samples (Figure 5e), as a clear sign of cell infiltration in the volume of the synthetic scaffold. In addition, the cell nuclei inside the Microatlas scaffolds, showed a conformation resembling an oblate ellipsoid (Figure 5). In many cases, adaptations in nuclear shape and structure may be related to the functionality of the cell: more deformable lobulated nuclei in neutrophils allow increased intercellular translocation,[51] as an example. In addition, as suggested by Thomas and colleagues,[52] collagen synthesis could better correlate with nuclear shape than with cell shape. In fact, Thomas and colleagues highlighted that 3D-patterned substrates resulted in the highest collagen I expression levels in cell culture. Thus, our 3D scaffold may elicit the production of collagen I inside each pore, consistently with a reduced tendency of formation of a fibrotic capsule as can be seen from the SHG microscopy images (Figures 5g,h and 6b,d). Overall, the SHG images indicates that the formation of collagen is limited to the surroundings of the Microatlas (see Figure 5g,h) and does not seem to correspond to the formation of a capsule, as would be the case if inflammatory response were elicited.[4] In vitro tests of SZ2080 in comparison to other hybrid organometallic polymers[53] clearly indicate that SZ2080 is biocompatible in vitro and has the potential for bioengineering applications. This is in agreement with the observation of other groups[23] who reported preclinical tests on SZ2080 microstructures implanted in the weight-bearing area of the medial femoral condyle in rabbits for up to 6 months. Although their microstructures were able to induce the chondrocytes differentiation, they did not provoke a marked foreign body reaction with infiltration of any inflammatory type cells, i.e., leukocytes and macrophages, as could be confirmed by a morphological analysis. No detectable formation of type-X collagen, a marker for fibrogenesis, was detected in their implanted samples, thus indicating limited or no fibrogenesis. However, no direct evaluation of macrophages into M1 or M2 states was reported on SZ2080[54] yet.

Our future work will be therefore focused on the development of a modified scaffold which will allow the observation of collagen I and its measurement in vivo, now partially masked by the stronger autofluorescence contribution of the Microatlas grid, passing through the 400/40 nm spatial filter.

Therefore, our device was able to stimulate cell infiltration also promoting a more oriented tissue architecture. The latter facilitated diffusion-based mass transfer to reduce the ischemic injury, often encountered in cell aggregates or even in cell transplantation,[55] during neoangiogenic regeneration. Despite literature evidences that 20 μm sized pores may allow functional neoangiogenesis,[56] we could not detect blood vessels inside the Microatlas scaffold at the two time-points considered (Figure 5g,h). This result is not a matter of incubation time since, by inspecting the devices one week after implantation (day 7), we did not detect a developed neovascularized network inside the Microatlas and the scaffolds resulted damaged by vessels with a diameter >150 μm (Figure S2, Supporting Information). Therefore, the high cellular density reached in and around the Microatlas probably stimulated neovascularization outside the scaffold with capillaries of increasing size which progressively infiltrated the synthetic microgrids. This is consistent with the observation that only microstructures with bigger pores, in the order of a 30–40 μm, allow a maximal vascularization and minimal fibrous encapsulation.[56] Therefore, in future work we will design a scaffold with an enlarged pore size to promote and visualize neovascularization inside the Microatlas scaffold grids.

3. Conclusions

In order to fabricate a miniaturized imaging window with a 3D microscaffold that can be implanted in vivo, we have precisely characterized the employed photoresist, SZ2080, in terms of

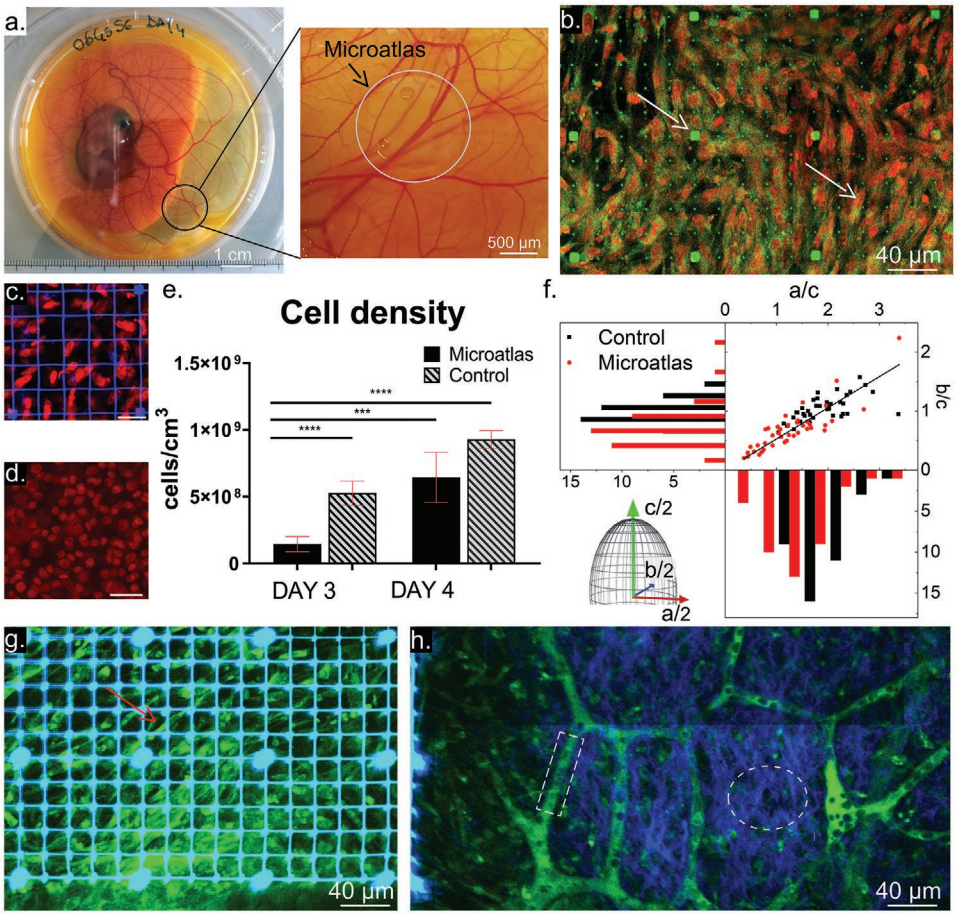

Figure 5. Validation of the Microatlas ex ovo. a) Chicken embryo 4 d after the implant. The embryo was cultured following a Petri-in-Petri approach. The Microatlas device (black circle) was implanted into the lower part of the chorioallantoic membrane (CAM), in proximity of a blood vessel bifurcation. On the right, a zoomed image of the CAM shows the Microatlas edges, highlighted by a white circle. b) Confocal microscope multistack image of the implanted device showing the autofluorescence signal (green) mainly arising from the microgrid pillars (white arrows) and from the cellular cytoplasm and the fluorescence of the DRAQ5 dye (red) that stains the cell nuclei. No fluorescence contribution of the Atlas grid is detectable into the DRAQ5 emission channel. c,d) Examples of confocal microscope images (100×100 µm^2 field of view) of the implanted Atlas (Panel (c)) and of a control (Panel (d)) region taken from the same chicken embryo, used to quantify the cellular density and the nuclear shape factor. The white bar is 20 µm. e) Quantification of the cellular density in the implant regions and the control area at day 3 and day 4 after the implant. The rate of the increase of cellular density in the Microatlas is larger than that of the control regions (***: $p < 0.001$; ****: $p < 0.0001$). f) Correlation plot of the major versus the minor planar axes of the cell nuclei normalized to the vertical one. The solid line is the linear best fit to all the data with slope 0.53 ± 0.02 ($R = 0.953$). Cells into the Microatlas resemble an oblate ellipsoid. Frequency counts of the ratios are represented along the major axes. g) The label free two-photon microscope multistack acquisition shows the presence of cells inside the microgrid pores. A 535/50 nm filter is exploited to select the cells autofluorescence (green). The microgrid autofluorescence (cyan) leaks also through the 400/40 nm filter used to detect SHG. h) Label free two-photon autofluorescence and second harmonic generation (SHG at 400 nm) image of an unimplanted region near the Microatlas (visible in the leftmost side of the panel). Collagen type I, in blue (400/40 nm), is visible (white circle on the right side of the image) within a newly formed capillary network (in green at 535/50 nm) infiltrating the areas surrounding the Microatlas scaffold (slightly visible on the left edge of this panel). A newly formed vessel is highlighted by a white box. The black dots inside the vascular network are red blood cells.

elastomechanical and fluorescence behavior. Then, we designed the miniaturized scaffold and all its features, the Microatlas, which was two-photon polymerized and implanted in living chicken embryos to prove the efficacy of that device in an in vivo context in terms of imaging capability and quantified cellular density.

Both mechanical and autofluorescence intensity investigations highlighted the planar raster spacing, R as the most important parameter in tuning the mechanical and spectroscopic features of the polymeric structure. These results allowed us to develop an optimized miniaturized imaging window that can be implanted in the CAM of living chicken embryos, and act as an effective model to quantify aspects of the host response to implantation of an artificial device in vivo. That window chamber allowed to define functional time-points (day 3 and day 4 after the implantation) that we used to visualize the occurring reaction by means of fluorescence laser microscopy. The microgrids constituting the Microatlas guided the formation of a newly formed tissue (Figures 5h and 6c), permitting a confined regeneration, allowed for repeated microscopy observations in

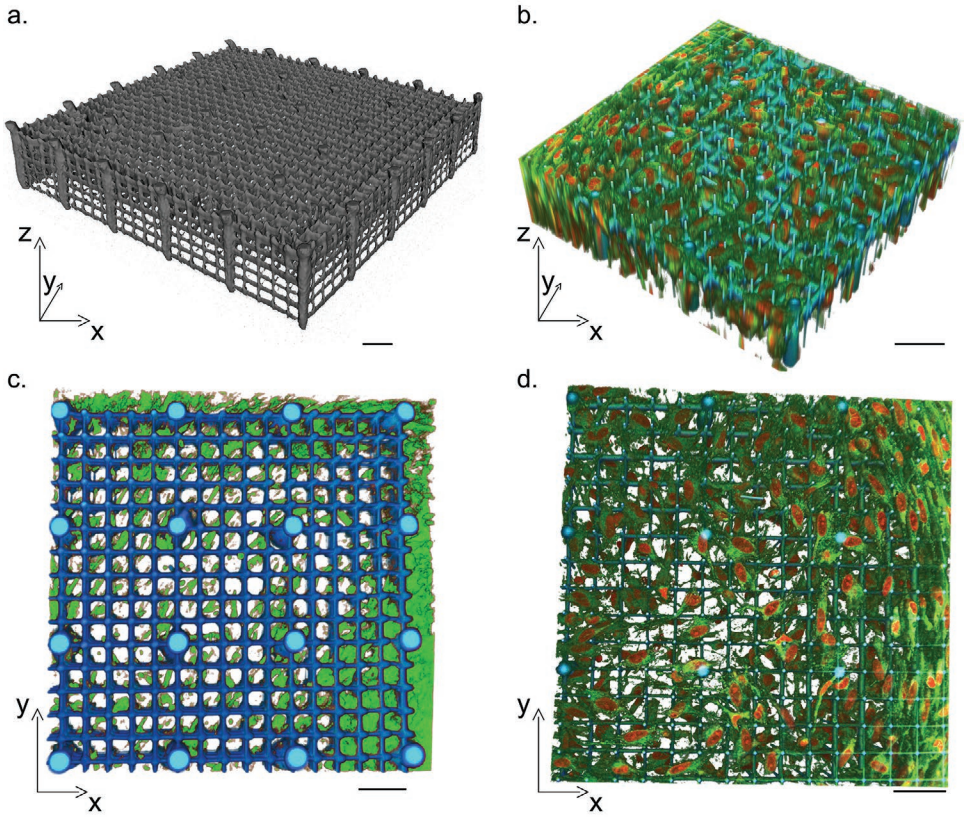

Figure 6. Distribution of cells within the Atlas. 3D renderings, reconstructed from fluorescence microscopy images. a) Rendered image from a multistack two-photon microscope acquisition. The device was imaged before the implantation. b) Confocal fluorescence reconstructed 3D image of an implanted device. Cells are clearly infiltrating the microgrid pores. Green indicates autofluorescence signal of cells, red the cell nuclei (DRAQ5 fluorescent dye). c) Two-photon microscopy 3D reconstruction. Upper view of the cells infiltrating the Microatlas, in green autofluorescence signal (535/50 nm) of the embryo tissue inside the microgrid, in blue signal collected in the 400/40 nm channel, corresponding to residual fluorescence of the photoresist. No evidence of collagen formation can be seen on this channel within the Microatlas. d) Confocal microscopy 3D reconstruction. Upper view of the cells infiltrating the Microatlas; in green autofluorescence signal of the cellular bodies, in red (DRAQ5 fluorescent dye) cell nuclei. The images in panels (b)–(d) were acquired at the experiment endpoint (day 12). Scale bars: 100 µm.

the same recipient position at different time points and finally, they allowed for correction of optical aberrations (Figure 4e,f). Indeed, the repositioning of the implanted chip in the microscopy field of view is fast and effective since the planar landmarks (Figure 4b) enable the operator to identify the *X*-axis orientation and the cone cross-sectional area allows to measure the position of the imaging plane along the *Z*-axis. The cellular infiltration inside the scaffolds was proved (Figure 6b,d) with a fast growth rate within 24 h and the infiltrated cells nuclei highlighted a conformation resembling an oblate ellipsoid.

These promising results highlight the efficacy and reliability of the Microatlas platform, obtained by two-photon polymerization of the SZ2080 resin and thoroughly characterized in terms of mechanoelastic and spectroscopic properties, as an effective miniaturized imaging window for intravital fluorescence microscopy. The unique features of Microatlas are to encompass in a mm^2 area a single microfabricated structure that has a number of advantages from the point of view of tissue engineering and of optical inspection in vivo. From the tissue engineering point of view, the Microatlas is actively colonized by the host tissue, allows for angiogenesis and does not seem to elicit massive fibrotic reaction. From the point of view of in vivo test through optical imaging, the Microatlas, due to its autofluorescence under two-photon excitation, allows for repositioning of the sample in the optical microscope field of view for long lasting longitudinal studies, and constitutes a highly regular and easily recognized microstructure to be used as beacon for optical aberrations corrections. It is the purpose of the research team to exploit these unique features to devise implantable microdevices for the test of the inflammatory reaction to biomaterials in rodents and for the test of drugs or vaccines, on chicken embryos.

4. Experimental Section

Sample Preparation for Two-Photon Laser Polymerization: The photoresist employed for 2PP was the SZ2080,[31] a negative organic–inorganic biocompatible resin, extensively validated for cell culture.[13,57] About 35 µL of SZ2080 photoresist were deposited by drop casting on a 12 mm diameter circular glass coverslip (#1.5, Bio-Optica, Italy). The operation was performed always leaving a free external annuls on the glass substrate. This annulus has the role of assuring the correct holding inside the support. Samples were then baked at 105 °C for 60 min on an electrical hot plate (Stuart, Bibby Scientific, UK). Once the evaporation

of the solvent occurred, the photoresist reached a semi-solid state, thus preventing any unwanted sliding of the structures during the fabrication procedures. Moreover, the baking procedure allowed creating the initial chemical bonds between monomers and oligomers of the photoresist, preparing a starting substrate for the following laser-induced crosslinking.

Two-Photon Laser Polymerization Setup: 2PP fabrication was performed by a laboratory-made femtosecond Ytterbium (Yb) laser system, based on a cavity dumped mode-locked oscillator. The lasing wavelength was λ = 1030 nm, the pulse duration is ≅300 fs, the repetition rate 1 MHz, the pulse energy 1 µJ, resulting in a maximum average output power ≅ 1 W. The laser beam passed through a software controlled mechanical shutter (Uniblitz Electronics, LS Series, USA; maximum operative frequency ≅1 kHz) and was tightly focused by a plan-apochromat 100x oil immersion objective with numerical aperture (NA) 1.4, (Carl Zeiss, Germany) onto the photosensitive material, passing through the sample glass substrate (Figure 1b). The sample was mounted on an aluminum circular support connected to a gimbal mechanical system (Gimbal Mounts 100, Thorlabs, USA). The gimbal system presents an inner threaded hole, which allowed to fabricate various sample-holder, just fitting the cavity, giving the sample-holder a wide versatility. The sample holder-gimbal complex was mounted onto a planar (*X*, *Y*) brushless motion stage (ANT130XY Series, Aerotech, USA). The *Z*-direction, instead, was controlled by a motorized stage, balanced by two air compressed pneumatic pistons (ANT130LZS Series, Aerotech, USA), which counterbalance the gravity and avoid vibrations. These three stages were controlled via software (Automation 3200 CNC Operator Interface, Aerotech, USA) and equipped with a feedback position and velocity control system having a resolution in the order of nm. A red-light emitting diode illumination was positioned under the sample-holder, in the central cavity of the gimbal, allowing the visualization during the writing process of the working area, as well as of the polymerized structures, through a complementary metal-oxide-semiconductor camera (DCC1545M, Thorlabs, Germany). The three-axes stages and all the other setup components were placed on a granite arch (ZALI, Italy), in turn placed above a pneumatic vibration isolator workbench (Newport, Stabilizer, High Performance Lamina Flow Isolator, I-2000 Series, USA).

After the laser fabrication process, the samples were developed to remove all the unpolymerized photoresist. Briefly, the samples glass surface was soaked for 20 min in a glass beaker filled with a 50% v/v 2-pentanone, 50% v/v isopropyl alcohol solution (Sigma-Aldrich, USA). Then, the samples were washed with abundant isopropyl alcohol and then gently dried by room temperature Nitrogen.

Physicochemical Resin Characterization: The Young's Modulus of the polymerized SZ2080 structures was measured by means of a microindenter hardness testing machine (Fisherscope H100 VP XY, Helmut Fisher, Italy) mounting a Vickers tip, while fluorescence intensity properties of the resin were studied by using an inverted confocal microscope (Nikon A1R+, Nikon, Japan). To perform these measurements, micrometric bulk structures (Figure 2a) were fabricated by polymerizing raster-written lines spaced in the horizontal and the vertical directions by a raster parameter *R*, and a slicing parameter *Z*, respectively, using a fixed writing speed of 3 mm s^{-1} (Figure 2e,f). The overlap region between the polymerized lines, determined by the choice of *R* and *Z*, was adopted as a fabrication parameter that affects the density of the polymerized structures. The dependence of the Young's Modulus was studied on three parameters: laser power, *P* (4 mW ≤ *P* ≤ 6 mW), and the line spacing parameters *Z* (*Z* = 0.5, 1.0, and 1.5 µm) and *R* (0.15 µm ≤ *R* ≤ 0.95 µm, 0.2 µm step). *Z* was kept below *Z* = 2.0 µm, as this was found to be the maximum spacing that allowed to maintain the overall structure stability.

The geometry of the bulk samples was a parallelepiped structure with size 150 × 150 × 20 μm^3 for microindentation experiments or 10 × 10 × 10 μm^3 for fluorescence experiments. Five replicas of these structures were fabricated with different combinations of *P*, *Z*, and *R* parameters on a single circular glass coverslip, 12 mm in diameter. Nine different coverslips with a total of 45 cubes were investigated and the whole procedure was replicated. Each parallelepiped was indented in five different areas (Figure 2a), to achieve a homogenous measurement, with a load of 1000 nN maintained for 10 s, followed by an unload phase. For the fluorescence experiments, all the bulk structures were fabricated on a single glass coverslip.

The microstructures used for fluorescence characterization were coupled to a rectangular microscopy glass slide (30 × 22 mm, 1#, ThermoFisher, USA) with 5 µL of Mowiol 4-88 (Sigma-Aldrich, USA). The samples were stored in a lightproof box for 24 h at room temperature. To perform optical sectioning of the inspected volume, acquisitions were made by confocal microscopy serially using four different laser channels, with wavelengths of 408, 488, 561, and 640 nm and an oil-immersion 60x, NA 1.4, objective. All the data were processed both with Fiji-ImageJ (National Institute of Health, USA) and Matlab (MathWorks, USA). Fluorescence 3D imaging was done on 512 × 512 µm and 43 vertical volumes. Six linear regions of interest (ROIs) with ≈9 µm size and a mutual spacing of 3 µm, centered with respect the bulky structure and forming a hashtag shape with three lines along each axis, were chosen on the XY plane and repeated along the vertical *Z*-axis on three planes mutually spaced by 3 µm for a total number of 18 ROIs per cube. Boundary fluorescence contributions were neglected to avoid a misleading signal arising from densified bulk cube borders due to the fabrication process. The intensity profiles were processed in Origin (OriginLab, USA). Considering spectroscopic emission of the bulk structures, the spectrum was averaged on four linear ROIs traced along the *Y*-axis at the center of the cubic bulky structures. The cubes were serially excited with all the available laser lines. Then, all the measurements were replicated on new polymerized samples, as an experimental duplicate. The data homogenous distribution has been validated by means of analysis of variance test in all cases.

The Chick-Embryo Implantation: Groups of 12–24 fertilized eggs were collected per week from a local farm (L'orto in casa ss., Correzzana, Italy) and stored in a dark cold room at the temperature of 10–15 °C. The eggs were dry washed with a brush and then stored in clean eggcup, blunt-end down. Fertilized chicken eggs can be stored at ≈13 °C up to 5 d before incubation without initiating development with a negligible degradation.[58] Twelve eggs were incubated per experiment in the programmable incubator Automatic REAL-12 (Borotto, Italy), at constant temperature and with the rotational stimulus, needed to start the embryonic development. The humidity ratio (HR) was controlled by an electronic modular system (model: SIRIO, Borotto, Italy) directly connected to the incubator. The incubation parameters were: HR = 45%, *T* = 37.7 °C, rotational motion activated from the beginning of the process (see the Supporting Information). The Microatlas implantation in ovo occurred at the 8th day of incubation ex ovo and was performed under a sterile cabinet. Control specimens (i.e., nontreated embryos) were implanted with a sterile circular glass coverslip, free from any microfabricated structures. At the end of the experiment all the albumen content was removed and quickly substituted by formalin 4% (≈40 mL) assuring to cover completely the embryo. Then, the tissue portion was placed in a fridge at 4 °C to complete the fixing procedure, which lasted 72 h. Once formalin fixed, the embryo was washed three times in saline solution and stocked at 4 °C in phosphate buffered saline. Both implanted and control regions were extracted after washing procedure. None of the embryos used in this study reached the 14th embryonic incubation day, thus they could be used for experimentation without ethical restrictions or prior protocol approval.

Fluorescence Processing and Data Analysis: Cells nuclei staining was performed with the far-red nucleus fluorescent probe, DRAQ5 (AB1084104, Abcam, Italy) with excitation peak of 647 nm and emission spectrum between 665 and 681 nm, in a concentration 0.2% v/v (see the Supporting Information). Lastly, the sample was mounted with 30 µL of the embedding solution Mowiol 4-88 on a rectangular microscopy glass slide (30 × 22 mm^2, 1#, ThermoFisher, USA). The samples were then stored for 24 h at room temperature or 72 h at 4 °C.

Ex vivo and in vivo Microatlas images were processed to obtain the mean cellular density and the distribution of the characteristic nuclei size and draw a comparison between three implanted and three nonimplanted samples. On the far-red channel the fluorescence of the nuclear dye DRAQ5 arose, thus the nuclei were manually segmented to obtain

the characteristic sizes. For cell density quantification, two different time points (day 3 and day 4 after implantation) were considered. Six random ROIs, 100 × 100 μm^2 in size, were inspected both in the three independent Microatlas microgrids and in the control samples. The height of the inspected volume varied in the range 15–35 μm, so to assure the full 3D reconstruction of the cells in the volume. The cells were quantified by using the ImageJ Multipoint tool, manually selecting each cell throughout the entire volume and summing up the number of counts (cells) for each ROI. The cell density of each sample (Microatlas and control) was calculated assuming a homogeneous distribution of the cells along the vertical coordinate as follows

$$\text{Cell density} = \frac{\text{Cell number}}{\text{Volume}} \quad (1)$$

For the nuclei conformation analysis, about 80 cells were manually segmented from confocal fluorescence images taken on three implanted and three control areas. Then, the characteristic length, the area, and the volume of each nucleus were inspected and determined.

The Microatlas fluorescence acquisitions were performed either by confocal microscopy or two-photon excitation and SHG microscopy (see the Supporting Information). Multiple plane images were acquired at 512 × 512 and 1024 × 1024 pixel^2 resolution (spacing along the optical axis = 1 μm) using the 408 and 640 nm laser lines and a 40x long working distance water-matched objective, NA = 1.15.

Supporting Information

Supporting Information is available from the Wiley Online Library or from the author.

Acknowledgements

This research has received funding from the European Union under the Horizon 2020 research and innovation program (G.A. No. 964481 – IN2SIGHT); the Italian Ministry of University and Research (MUR) under the grant program MIUR-FARE-2016 (G.A. No. R16ZNN2R9K – BEYOND); Politecnico di Milano, Fondazione Social Venture Giordano Dell'Amore, Cariplo Factory, Fondazione Bassetti and Fondazione Triulza (project Switch to Product 2020).

Open access funding provided by Universita degli Studi di Milano-Bicocca within the CRUI-CARE Agreement.

Conflict of Interest

The authors declare no conflict of interest.

Data Availability Statement

The data that support the findings of this study are available from the corresponding author upon reasonable request.

Keywords

3D-microstructured scaffolds, confocal microscopy, elastomechanics, ex ovo implant, in vivo implant, intravital imaging windows, two-photon imaging, two-photon polymerization

Received: June 1, 2021
Revised: January 9, 2022
Published online:

[1] M. D. Menger, H. A. Lehr, *Immunol. Today* **1993**, *14*, 519.
[2] G. L. Wied, P. H. Bartels, M. Bibbo, H. E. Dytch, *Hum. Pathol.* **1989**, *20*, 549.
[3] L. Mulrane, E. Rexhepaj, S. Penney, J. J. Callanan, W. M. Gallagher, *Expert Rev. Mol. Diagn.* **2008**, *8*, 707.
[4] E. Mariani, G. Lisignoli, R. M. Borzì, L. Pulsatelli, *Int. J. Mol. Sci.* **2019**, *20*, 636.
[5] S. Franz, S. Rammelt, D. Scharnweber, J. C. Simon, *Biomaterials* **2011**, *32*, 6692.
[6] International Organization for Standardization (**2018**). Biological evaluation of medical devices—Part 6: Tests for local effects after implantation (ISO/EN standard No. 10993–6). Retrieved from https://www.iso.org/obp/ui#iso:std:iso:10993:-1:ed-5:v2:en
[7] J. Cohen, *J. Bone Jt. Surg.* **1959**, *41A*, 152.
[8] E. Dondossola, B. M. Holzapfel, S. Alexander, S. Filippini, D. W. Hutmacher, P. Friedl, *Nat. Biomed. Eng.* **2016**, *1*, 0007.
[9] M. W. Laschke, B. Vollmar, M. D. Menger, *Eur. Cells Mater.* **2011**, *22*, 147.
[10] C. Prunier, N. Chen, L. Ritsma, N. Vrisekoop, *Methods* **2017**, *128*, 52.
[11] J. Lee, M. Li, J. Milwid, J. Dunham, C. Vinegoni, R. Gorbatov, Y. Iwamoto, F. Wang, K. Shen, K. Hatfield, M. Enger, S. Shafiee, E. McCormack, B. L. Ebert, R. Weissleder, M. L. Yarmush, B. Parekkadan, *Proc. Natl. Acad. Sci. U. S. A.* **2012**, *109*, 19638.
[12] C. Maibohm, O. F. Silvestre, J. Borme, M. Sinou, K. Heggarty, J. B. Nieder, *Sci. Rep.* **2020**, *10*, 8740.
[13] M. T. Raimondi, S. M. Eaton, M. Laganà, V. Aprile, M. M. Nava, G. Cerullo, R. Osellame, *Acta Biomater.* **2013**, *9*, 4579.
[14] C. Momma, U. Knop, S. Nolte, *Prog. Biomed. Res.* **1999**, *4*, 39.
[15] F. Sima, K. Sugioka, R. M. Vázquez, R. Osellame, L. Kelemen, P. Ormos, *Nanophotonics* **2018**, *7*, 613.
[16] M. T. Raimondi, S. M. Eaton, M. M. Nava, M. Laganà, G. Cerullo, R. Osellame, *J. Appl. Biomater. Biomech.* **2012**, *10*, 56.
[17] C. N. LaFratta, J. T. Fourkas, T. Baldacchini, R. A. Farrer, *Angew. Chem., Int. Ed. Engl.* **2007**, *46*, 6238.
[18] A. Zeynali, M. Marini, G. Chirico, M. Bouzin, M. Borzenkov, L. Sironi, L. D'Alfonso, P. Pallavicini, V. Cassina, F. Mantegazza, F. Granucci, L. Marongiu, D. Polli, A. De la Cadena, M. Collini, *Adv. Opt. Mater.* **2020**, *8*, 2000584.
[19] S. Wu, J. Serbin, M. Gu, *J. Photochem. Photobiol., A* **2006**, *181*, 1.
[20] T. Baldacchini, V. Nuñez, C. N. LaFratta, J. S. Grech, V. I. Vullev, R. Zadoyan, in *Proc. SPIE 9353, Laser 3D Manuf. II* (Eds: H. Helvajian, A. Piqué, M. Wegener, B. Gu), SPIE, San Francisco, USA **2015**, p. 93530W.
[21] Z. Bayindir, Y. Sun, M. J. Naughton, C. N. LaFratta, T. Baldacchini, J. T. Fourkas, J. Stewart, B. E. A. Saleh, M. C. Teich, *Appl. Phys. Lett.* **2005**, *86*, 064105.
[22] F. Burmeister, S. Steenhusen, R. Houbertz, U. D. Zeitner, S. Nolte, A. Tünnermann, *J. Laser Appl.* **2012**, *24*, 042014.
[23] J. Mačiulaitis, M. Deveikytė, S. Rekštytė, M. Bratchikov, A. Darinskas, A. Šimbelytė, G. Daunoras, A. Laurinavičienė, A. Laurinavičius, R. Gudas, M. Malinauskas, R. Mačiulaitis, *Biofabrication* **2015**, *7*, 015015.
[24] A. Ovsianikov, M. Malinauskas, S. Schlie, B. Chichkov, S. Gittard, R. Narayan, M. Löbler, K. Sternberg, K.-P. Schmitz, A. Haverich, *Acta Biomater.* **2011**, *7*, 967.
[25] L. Pertoldi, V. Zega, C. Comi, R. Osellame, *J. Appl. Phys.* **2020**, *128*, 175102.
[26] C.-S. Shin, T.-J. Li, C.-L. Lin, *Micromachines* **2018**, *9*, 615.
[27] A. Žukauskas, I. Matulaitienė, D. Paipulas, G. Niaura, M. Malinauskas, R. Gadonas, *Laser Photonics Rev.* **2015**, *9*, 706.
[28] J. Song, C. Michas, C. S. Chen, A. E. White, M. W. Grinstaff, *Adv. Healthcare Mater.* **2020**, *9*, 1901217.
[29] J. Bauer, A. Guell Izard, Y. Zhang, T. Baldacchini, L. Valdevit, *Adv. Mater. Technol.* **2019**, *4*, 1900146.

[30] M. H. Tong, N. Huang, W. Zhang, Z. L. Zhou, A. H. W. Ngan, Y. Du, B. P. Chan, *Sci. Rep.* **2016**, *6*, 1.
[31] A. Ovsianikov, J. Viertl, B. Chichkov, M. Oubaha, B. MacCraith, I. Sakellari, A. Giakoumaki, D. Gray, M. Vamvakaki, M. Farsari, C. Fotakis, *ACS Nano* **2008**, *2*, 2257.
[32] P. Danilevicius, *J. Biomed. Opt.* **2012**, *17*, 081405.
[33] M. T. Raimondi, M. M. Nava, S. M. Eaton, A. Bernasconi, K. C. Vishnubhatla, G. Cerullo, R. Osellame, *Micromachines* **2014**, *5*, 341.
[34] G. Flamourakis, A. Kordas, G. D. Barmparis, A. Ranella, M. Farsari, *Opt. Mater. Express* **2021**, *11*, 801.
[35] L. Russo, T. Russo, C. Battocchio, F. Taraballi, A. Gloria, U. D'Amora, R. De Santis, G. Polzonetti, F. Nicotra, L. Ambrosio, L. Cipolla, *Carbohydr. Res.* **2015**, *405*, 39.
[36] Y.-R. V. Shih, K.-F. Tseng, H.-Y. Lai, C.-H. Lin, O. K. Lee, *J. Bone Miner. Res.* **2011**, *26*, 730.
[37] T. Zandrini, O. Shan, V. Parodi, G. Cerullo, M. T. Raimondi, R. Osellame, *Sci. Rep.* **2019**, *9*, 11761.
[38] O. Jonas, H. M. Landry, J. E. Fuller, J. T. Santini, J. Baselga, R. I. Tepper, M. J. Cima, R. Langer, *Sci. Transl. Med.* **2015**, *7*, 284ra57.
[39] S. Bhagavatula, D. Thompson, S. W. Ahn, K. Upadhyaya, A. Lammers, K. Deans, C. Dominas, B. Ferland, V. Valvo, G. Liu, O. Jonas, *Cancers* **2021**, *13*, 653.
[40] G. Liu, V. Valvo, S. W. Ahn, D. Thompson, K. Deans, J. W. Kang, S. Bhagavatula, C. Dominas, O. Jonas, *Int. J. Mol. Sci.* **2021**, *22*, 11752.
[41] M. A. A. Neil, R. Juskaitis, M. J. Booth, T. Wilson, T. Tanaka, S. Kawata, *J. Microsc.* **2000**, *200*, 105.
[42] D. Débarre, E. J. Botcherby, T. Watanabe, S. Srinivas, M. J. Booth, T. Wilson, *Opt. Lett.* **2009**, *34*, 2495.
[43] M. Collini, F. Radaelli, L. Sironi, N. G. Ceffa, L. D'Alfonso, M. Bouzin, G. Chirico, *J. Biomed. Opt.* **2019**, *24*, 025004.
[44] D. Ribatti, *The Chick Embryo Chorioallantoic Membrane in the Study of Angiogenesis and Metastasis*, Springer, Dordrecht, New York **2010**, pp. 1–130.
[45] T. I. Valdes, D. Kreutzer, F. Moussy, *J. Biomed. Mater. Res.* **2002**, *62*, 273.
[46] E. I. Deryugina, J. P. Quigley, *Methods Enzymol.* **2008**, *444*, 21.
[47] D. Ribatti, A. Vacca, L. Roncali, F. Dammacco, *Curr. Pharm. Biotechnol.* **2000**, *2*, 73.
[48] T. Schomann, F. Qunneis, D. Widera, C. Kaltschmidt, B. Kaltschmidt, *Stem Cells Int.* **2013**, *2013*, 960958.
[49] D. Ribatti, *Int. Rev. Cell Mol. Biol.* **2008**, *270*, 181.
[50] E. Dondossola, P. Friedl, *Nat. Rev. Mater.* **2021**, *7*, 6.
[51] K. N. Dahl, A. J. S. Ribeiro, J. Lammerding, *Circ. Res.* **2008**, *102*, 1307.
[52] C. H. Thomas, J. H. Collier, C. S. Sfeir, K. E. Healy, *Proc. Natl. Acad. Sci. U. S. A.* **2002**, *99*, 1972.
[53] M. Malinauskas, D. Baltriukiene, A. Kraniauskas, P. Danilevicius, R. Jarasiene, R. Sirmenis, A. Zukauskas, E. Balciunas, V. Purlys, R. Gadonas, V. Bukelskiene, V. Sirvydis, A. Piskarskas, *Appl. Phys. A* **2012**, *108*, 751.
[54] C. E. Witherel, D. Abebayehu, T. H. Barker, K. L. Spiller, *Adv. Healthcare Mater.* **2019**, *8*, 1801451.
[55] T. E. Robey, M. K. Saiget, H. Reinecke, C. E. Murry, *J. Mol. Cell. Cardiol.* **2008**, *45*, 567.
[56] L. R. Madden, D. J. Mortisen, E. M. Sussman, S. K. Dupras, J. A. Fugate, J. L. Cuy, K. D. Hauch, M. A. Laflamme, C. E. Murry, B. D. Ratner, *Proc. Natl. Acad. Sci. U. S. A.* **2010**, *107*, 15211.
[57] D. Ricci, M. Nava, T. Zandrini, G. Cerullo, M. Raimondi, R. Osellame, *Materials (Basel)* **2017**, *10*, 66.
[58] Y. Kim, K. C. Williams, C. T. Gavin, E. Jardine, A. F. Chambers, H. S. Leong, *Nat. Protoc.* **2016**, *11*, 937.